Research Toward Resolving Key Issues for ITER and Steady-State Tokamaks

D.N. Hill 1) for the DIII-D Team

1) Lawrence Livermore National Laboratory, Livermore, CA 94551

e-mail: hilldn@fusion.gat.com

Abstract. The DIII-D research program is addressing key ITER challenges and developing the physics basis for future steady-state tokamaks. Pellet pacing edge localized mode (ELM) control in the ITER configuration shows energy loss $\propto 1/f_{pellet}$ at frequencies up to 12x the natural rate, and complete ELM suppression with resonant magnetic perturbations (RMP) is now obtained at the q_{95} expected for ITER baseline scenario discharges. Long-duration ELM-free QH-mode discharges have been produced with ITER-relevant co-current neutral beam injection (NBI) using external n=3 coils to generate sufficient counter-I_P torque. ITER baseline discharges at β_N=2 and scaled NBI torque have been maintained in stationary conditions for more than 4 resistive times using electron cyclotron current drive (ECCD) for tearing mode (NTM) suppression and disruption avoidance; active tracking with steerable launchers and feedback control catch modes early and reduce the ECCD energy requirements. Disruption experiments with massive gas injection reveal runaway electron dissipation rates ~10x faster than expected and demonstrate the possibility of benign dissipation in ITER. Other ITER-related experiments show measured intrinsic plasma torque in good agreement with a physics-based model over a wide range of conditions, while first-time main-ion rotation measurements show it to be lower than expected from neoclassical theory. Core turbulence measurements show increased temperature fluctuations correlated with sharply enhanced electron transport when $\nabla T_e/T_e$ exceeds 2.5 m^{-1}. Near the separatrix in H-mode, data show the pedestal height and width growing between ELMs with ∇P at the computed kinetic-ballooning limit, in agreement with the EPED model. Successful modification of a neutral beam line to provide 5 MW of adjustable off-axis injection has enabled sustained operation at β_N~3 with minimum safety factors well above 2 accompanied by broader current and pressure profiles than previously observed. Initial experiments aimed at developing integrated core and boundary solutions demonstrated heat flux reduction using radiative edges and innovative divertor geometries (e.g., snowflake configuration).

1. Introduction

The DIII-D Research Program has made significant advances in developing the physics understanding and operational experience needed to ensure the success of ITER. By simulating candidate operating scenarios with increasing fidelity, this research addresses many of the research needs identified by ITER [1]. Targeted research aims to demonstrate relevant solutions and the scientific basis for avoiding and controlling transient events such as edge localized modes (ELMs) and disruptions which can limit ITER's reliability.

Many of the results reported here capitalize on several new DIII-D capabilities, including variable off-axis neutral beam injection (OANBI) for improved current and pressure profile control, real time steerable electron cyclotron current drive (ECCD) for tearing mode control, high rep-rate pellet injectors, shell pellets, and new diagnostics for validating predictive simulation. These capabilities enable DIII-D to serve as a research platform to qualify advanced operating modes for new superconducting long-pulse tokamaks and for ITER's steady-state mission.

The organization of this paper is as follows. Section 2 summarizes progress on developing ELM control for ITER and how improved understanding of the H-mode pedestal informs the research. In Sec. 3 we discuss progress on disruption mitigation and Sec. 4 covers research in support of the Q=10 ITER mission, including tearing mode control, QH-mode developments, and error field correction. Section 5 covers research directed towards developing predictive capability for burning plasma experiments (pedestal scaling, core transport including intrinsic rotation, and the H-mode threshold). Then in Sec. 6 we discuss results on Advanced Tokamak development using OANBI, concluding with a description of work producing integrated core-boundary solutions. Future research plans for DIII-D are briefly discussed in the final section.

2. ELM Control and the Physics of the Pedestal

ELM control is essential for ITER to achieve its fusion goals. DIII-D is developing three approaches to ELM control for ITER: ELM suppression by application of edge-resonant magnetic perturbations (RMP) [2,3], pellet pacing [4] to reduce transient heat loads by increasing ELM frequency, and naturally ELM-free QH-mode [5].

In recent experiments, complete ELM suppression for 3.5 s was obtained using an ITER-similar shape at ITER's baseline value I/aB=1.41 (q_{95}~3.4) and at low pedestal collisionality [6] (Fig 1). These experiments used a single row of internal coils (I-coil) to produce larger n=3 perturbations at the internal resonant surface, while broadly deposited ECCD around the q=2 surface avoided internal MHD modes (fishbones, sawteeth, and tearing modes) to maintain complete suppression. ELM mitigation with n=2 RMPs at low ITER-like collisionality has also been demonstrated, extending previous results from ASDEX-U showing suppression using n=2 at high collisionality [7].

ELM pellet pacing experiments using small (0.9–1.3 mm) deuterium pellets demonstrate increased ELM frequency, with peak divertor heat flux decreasing by at least $1/f_{pellet}$ [4]. Pellets were injected at 60 Hz into an ITER-shaped plasma with β_N=1.8 at q_{95}=3.5, achieving 12x higher ELM frequency and a strong reduction in impurity content with little impact on density and energy confinement (Fig. 2). In these experiments, one 40 Hz and one 20 Hz injector were used to inject pellets at ~150 m/s on the low-field side midplane and through the outer scrape-off layer (SOL) just above the X-point (similar to the planned ITER geometry). The pellets trigger ELMs when they reach half way into the H-mode pedestal, and high speed imaging of the pellets shows formation of filaments near the pellet, suggesting that ELMs are triggered by local triggering of the instability and not by a general increase in overall pedestal density, in agreement with pellet simulations using the JOREK code used to predict penetration in ITER [8].

Robust predictive capability for RMP ELM control in ITER is a primary goal for DIII-D experiments. The EPED model [9] of pedestal structure provides an intuitive framework for

Fig. 1. Single-row n=3 RMP ELM suppression at ITER I/aB and low v^* with ITER-like shape.
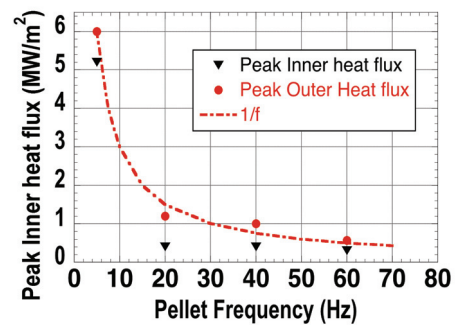

Fig. 2. ELM pacing with small deuterium pellets showing peak heat flux decreasing with pellet frequency.

Fig. 3. H-mode pedestal evolution between ELMs. Red-data; Lines-EPED simulation.

experiments. New high-resolution edge measurements show how the H-mode pedestal evolves during an ELM cycle (Fig. 3). Both the pedestal width and pedestal-top pressure

grow steadily in time, moving along a trajectory of constant pressure gradient that matches the calculated Kinetic Ballooning Mode (KBM) stability limit [10]; fluctuation diagnostics show evidence of high frequency modes in this region with characteristics consistent with KBMs [11]. When the evolving pedestal crosses the Peeling-Ballooning mode pressure limit, an ELM occurs and the cycle repeats. Thus, mechanisms which prevent the pedestal height or width from growing should, in principle, suppress ELMs.

Unravelling the edge plasma response to applied RMPs in ELM control experiments is challenging. Experiments featuring temporal modulation of the $n=2$ and $n=3$ RMP toroidal phase and amplitude provide new insights. The data reveal a complex plasma response that includes helical displacements at the edge combined with modulation in the density, temperature, and fluctuation amplitude near the top of the pedestal where the electron perpendicular drift velocity is zero [6]. New tangential X-point soft x-ray image differencing locked to the RMP modulation shows the existence of filamentary structures near the separatrix (Fig. 4), similar to both vacuum-field calculations and two-fluid simulation of the plasma response [12]. The edge density response to the RMP is nearly independent of q_{95}, while the edge T_e responds most strongly when q_{95} is within the suppression window. Long wavelength density fluctuations increase rapidly in the outer regions of the plasma following application of the RMP, which may explain the increased particle transport [13]. Overall, the full suite of observations is consistent with the picture that the RMP generates a strong resonant response near the top of the pedestal, increasing transport to limit the pedestal width, thereby averting the ELM.
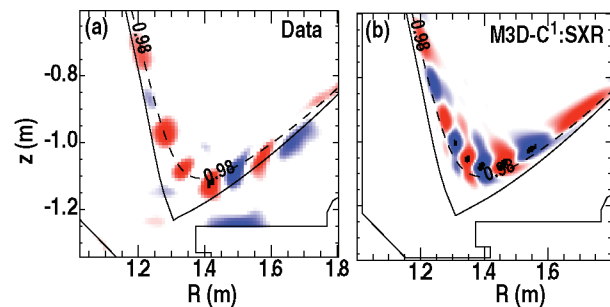

Fig. 4. Tangential SXR X-point imaging data showing filamentary structure near the X-point, as compared to simulation. Colors indicate relative phase compared to modulation (±).

3. Disruption Mitigation

Disruptions in ITER are expected to generate large runaway electron (RE) currents compared to present tokamaks. While massive gas injection (MGI) will mitigate the thermal quench, it will be far more challenging for MGI to prevent REs by raising density to a critical value [14]. Experiments in DIII-D using MGI, shattered argon pellets, and shell pellets have so far reached 20% of the scaled target value [15]. Even so, MGI can significantly reduce the potential damage from RE in ITER by dramatically increasing dissipation.

Systematic study of RE dynamics and dissipation in DIII-D shows that passively stabilized RE beams dissipate benignly against the inner wall while drifting vertically over many milliseconds, smoothly decaying from the outside-in until the innermost energetic core (~0.3 m dia.) is finally in contact with the wall [16]. At the end, wall impurities increase rapidly causing the RE beam to disrupt, at which point data shows most of the remaining magnetic energy is safely converted to low energy plasma current.

Fig. 5. Enhanced RE dissipation with high-Z gas injection.

High-Z impurity gas injection (argon and neon) during or after RE formation strongly increases the dissipation rate (Fig. 5), in some cases allowing complete benign dissipation of up to 600 kA RE beams even without active position control. Overall, the dissipation rate is

as much as 10x higher than expected from e-e collisions only, and the measured RE energy distribution shows a much larger fraction of lower-energy electrons than expected from avalanche theory and e-e collisions alone [15]. With active position control, the RE beam current ($I_{RE} \leq 300$ kA) can be maintained out to the V-S limit of the ohmic solenoid or until the current is smoothly ramped to zero, allowing precise loop voltage, electric-field, impurity spectroscopy, and density measurements under a variety of conditions [17].

Other disruption mitigation studies systematically examined the first-wall heat flux resulting from vertical displacement events (VDEs) in single-null discharges. High speed IR TV measurements showed that most of the heat flux was deposited on the inner wall near the divertor, independent of toroidal field direction; low shot-to-shot variation implies less than 30% toroidal variation. Prompt argon injection at the thermal quench reduced the divertor heat flux by 40%, though little reduction was observed if delayed by 25 ms.

4. Meeting ITER Performance Goals in the Burning Plasma Regime

The DIII-D research program places high priority on experiments which simulate planned ITER operating scenarios, using both co- and counter-I_p neutral beam injection to vary the scaled ITER-equivalent neutral beam torque and resulting rotation velocity. With strong co-current neutral beam injection, and feedback controlled $\beta_N \sim 2$, ITER-shaped plasmas at $I/aB=1.4$ reached and maintained stationary conditions free of tearing modes for $>10\tau_R$. However, small changes in β or a small reduction in co-current neutral beam injection (NBI) torque and plasma rotation result in increased tearing mode activity. Adding ~ 3 MW of ECCD broadly deposited near the $q=3/2$ surface (~ 30 kA total drive current) suppressed the tearing modes even as the NBI torque was reduced to the scaled ITER equivalent of <1 Nm, allowing stationary conditions to be maintained for more than 4 resistive times [18] (Fig. 6). Subsequently, long-pulse ITER baseline scenario demonstration discharges featuring low-torque start up and ramp up were obtained.

DIII-D simulation of the ITER hybrid or advanced inductive (AI) scenario, which features higher β with improved stability at higher q_{95} than the ITER baseline case, demonstrated successful low-torque ramp up to stationary conditions [19]. These discharges feature $\beta_N \sim 3$, $H_{98} \sim 1$, $q_{95} \sim 4$, and fusion gain $G=\beta_N H_{89}/q_{95}^2 \sim 0.35$ roughly equivalent to ITER $Q=10$ ($G=0.4$). At constant β_N, the plasma rotation velocity is reduced with lower NBI torque, and confinement is degraded significantly (H_{98} drops from 1.5 typical of AI plasmas to 1.0). Similar to the ITER baseline scenario

Fig. 6. ITER baseline simulation with low rotation. (a) β_N & l_i, (b) torque and ECCD power, (c) density.

experiments described above, at reduced torque the plasma is more susceptible to neoclassical tearing modes which generally slow and lock. Application of ~ 1 MW of ECCD near the $q=2$ surface suppresses these modes, allowing stable high performance operation ($\beta_N \sim 2.5$) even with zero net NBI torque and very low plasma rotation.

Research continued on developing the physics basis for another promising ITER operating mode, the ELM-free QH-mode [5]. Recent experiments using only external coils (*outside the toroidal field coils*) have produced stationary QH-mode discharges with low plasma rotation, extending the operating space to include co-current NBI torque providing 3–4 times the torques scaled from the ITER beams [20]. The strong edge rotational shear needed for QH-mode access was maintained using counter-I_p torque arising from neoclassical

toroidal viscosity (NTV) produced by applying non-resonant magnetic fields (NRMF). Best results have been obtained with $n=3$ external coils (Fig. 7), though $n=3$ NRMF using internal coils also works well. These QH-mode plasmas exhibit excellent confinement at low torque (H_{98y2}=1.3) and operate stably at $\beta_N \sim 2$ with low collisionality ν^*_{ped} =0.05 at q_{95}=4.7 (I/aB=1) with nearly zero core rotation [21]. Higher current discharges with G=0.4 have been obtained at q_{95}=3.4 as well. The fact that QH-mode can be obtained robustly over a wide range in heating power using NRMF to produce the rotational edge shear may make it an attractive operating mode for ITER.

Improved tearing mode control is now available on DIII-D. Actively tracking the q=2 and q=3/2 surfaces and applying ECCD when NTMs are first detected reduces the power required to suppress tearing modes altogether, confirming the feasibility and benefit for such feedback control in ITER. Several integrated control schemes have been developed and tested, which combine real-time motional Stark effect (MSE) measurements to locate the target q-surface, fast steering mirrors on the EC launchers, and a model-based aiming algorithm which corrects for beam diffraction in the plasma [22]. Both 3/2 and 2/1 neoclassical tearing modes have been suppressed (2/1 suppression shown in Fig. 8), and early application reduces the required power significantly (to below 1 MW, cf above) as expected [23]. In extreme cases where the tearing mode grows large enough to lock, experiments have shown that 3D field coils can be used to align the toroidal location of the O-point with ECCD deposition to stabilize the mode and avoid disruption.

Fig. 7. QH-mode maintained with ITER-like co-I_p NBI torque by application of $n=3$ NRMF. Edge rotation counter to NBI torque.

Fig. 8. ECCD NTM Control. (a) Mirror tracking, (b) ECCD tracking q=2 surface, (c) mode suppression during ECCD pulse.

Disruptive tearing modes can also be destabilized by fast-ion stabilized sawteeth, if large enough. Experiments using electron cyclotron current drive (ECCD) to increase the magnetic shear near the q=1 surface have demonstrated control of the fast-ion stabilized sawtooth size, reducing it to allow operation at β_N>3 without large 2/1 tearing modes [24], an important demonstration of the physics basis for this approach in ITER.

It will be important for ITER to obtain good error field correction (EFC) to achieve its goals. Error field correction experiments utilizing large proxy n=1 error fields from either external coils or the ITER Test Blanket Module (TBM) mockup coil [25] show that correcting only the lowest-order error field components can introduce strong residual rotational drag which reduces stability and confinement. In one experiment, the TBM
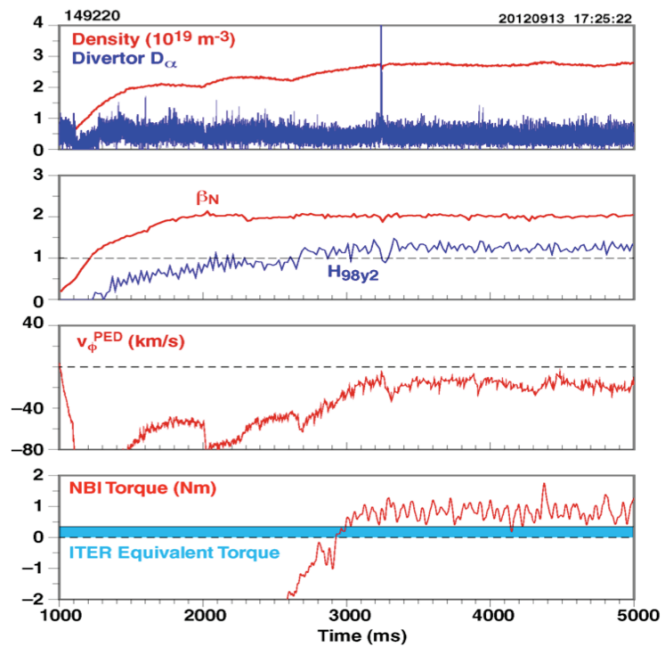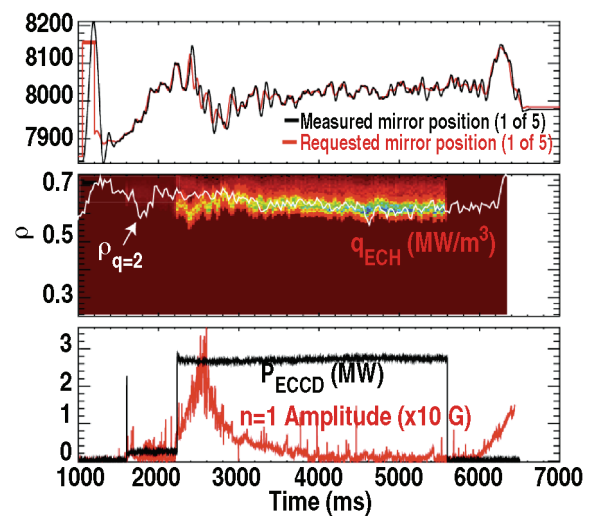
mockup coils introduce a single highly localized field perturbation, while in the other (Fig. 9), the external C-coils introduce a more purely $n=1$ error; internal coils (the I-coils) provide the error field correction in either case [26]. The TBM experiments utilizing improved $n=1$ EFC, still recover only ~25% of the rotation reduction previously observed with uncompensated $n=1$ error fields due to the TBM [27]. Modeling with the IPEC code explains results for the n=1 proxy error field experiment through an increase in non-resonant fields and rotation braking when the low-order resonant correction is applied.

These results suggest that optimal correction may require ITER to maintain flexibility in its EFC coil set to produce multiple poloidal harmonics, possibly including its ELM control coils in the mix, using measured plasma rotation to provide feedback control.

5. Developing Predictive Capability for Burning Plasma Experiments

Fig. 9. Optimized I-coil correction of $n=1$ error field showing 50% improvement in locked mode threshold.

Predicting the temperature at the top of the pedestal is key to predicting performance in ITER. Coordinated experiments involving DIII-D, C-Mod, and NSTX produced high resolution edge pedestal profile data which were compared against a number of theory-based simulation codes [28]. Adding the data from C-Mod doubled the range over which the EPED model correctly predicts the pedestal height without recourse to adjustable or fitted parameters. With a present database of 270 discharges from 5 tokamaks (Fig. 10), there is increased confidence that the EPED model can be used to predict the pedestal pressure height in ITER to within ~20%, using no fitted parameters. This model guides ELM mitigation experiments with RMPs, pellets, and QH-mode.

The DIII-D program carried out experiments to measure core transport stiffness in L-mode and H-mode discharges, and to further explore the theory-measurement discrepancy in L-mode edge transport. The critical gradient scale length for the onset of increased electron transport in L-mode discharges was measured using localized electron cyclotron heating (ECH) to vary the gradient scale lengths at mid-radius by a factor of 4 while changing the local heat flux a factor of 10; both power

Fig. 10. Comparison between EPED model pedestal height and measured values for 270 H-mode discharges from 5 tokamaks.

balance and heat pulse propagation showed similar responses, consistent with a sharp rise in transport when the gradient scale length $1/L_{Te} = \nabla T_e/T_e > 2.5$ m^{-1} [29], as shown in Fig 11. During these experiments, a sharp rise in local electron temperature fluctuations and a change in the $\tilde{n}\tilde{T}_e$ cross-phase coincident with the change in transport was observed for the first time [30].

In separate beam-heated H-mode discharges with nearly constant pedestal density and temperature (normally both rise with heating power), no sign of a critical gradient threshold for increased ion or electron transport is observed; inside ρ~0.5 electrons are less stiff than in
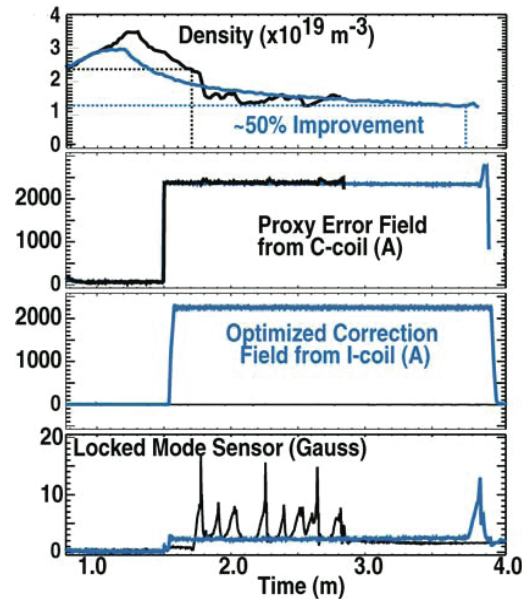
L-mode and ions are do not appear very stiff by comparison in agreement with both TGLF and full gyrokinetic simulations [31].

Other transport experiments yielded fluctuation measurements which may point to an explanation of the shortfall in gyrokinetic simulations of L-mode edge transport ($\rho \geq 0.7$) as compared to experiment. Data at lower current (higher q_{95}) show increased edge temperature and density fluctuations with a concomitant decrease in low frequency turbulent flow, as compared to the lower q_{95} companion case [32]; correlating large changes in both the shortfall and the turbulence with changes in the magnetic shear should help identify the physics changes required to improve the fidelity of simulations.

Plasma rotation, arising largely from neutral beam injection in present tokamaks, strongly benefits both transport and stability. However, in ITER it is expected that intrinsic torque arising from pressure gradients, neoclassical and 3D magnetic field effects and turbulent processes, will in large part determine its rotation due to its relatively large moment of inertia. Using co- and counter-NBI to apply a step change in NBI torque, the intrinsic torque as a function of radius has been inferred from the changes in the rotation profile, and from these data a simple physics-based model of intrinsic rotation has been developed. In the edge pedestal region data show that turbulent Reynolds stress alone is insufficient to explain the formation of a large intrinsic edge rotation layer. A model which includes edge thermal-ion orbit loss ($\propto \sqrt{T_i}$) and ∇P_{ped} describes measured intrinsic edge torque in DIII-D and NSTX H-mode plasmas, including Advanced Inductive discharges with much higher intrinsic torque [33]. This model predicts relatively low intrinsic torque in ITER (Fig. 12).

These studies have benefit from first-time simultaneous measurements of main ion and impurity ion (carbon) rotation profiles. These comparisons show differences (main ion velocity less than carbon-ion velocity) that are significantly lower than neoclassical predictions [34] in low-torque H-mode discharges. These results may have implications for transport in ITER, where rotational shear may be reduced.

The paradigm of flow-shear stabilization of edge turbulence following the H-mode transition is well documented, but the trigger for the L-H transition has remained elusive. Significantly, beam emission spectroscopy (BES) and microwave Doppler backscattering (DBS) show trends in turbulence and turbulent flows at the H-mode transition that mirror well-known density and magnetic field scaling of the H-mode power threshold, possibly revealing the underlying physics of the transition threshold for the first time [35]. Just prior to the transition, BES shows high frequency fluctuation amplitudes near the separatrix trending

Fig. 11. L-mode critical-gradient electron stiffness in DIII-D. (a) Change in electron heat flux and (b) in $\tilde{T}_e$.

Fig. 12. Predicted vs measured intrinsic torque for H-mode plasmas.

downward with increasing B_{tor}, while low frequency turbulent flow velocity shear increases at lower density ($P_{LH} \propto n^{0.7}B^{0.8}$), as shown in Fig. 13. In dithering H-mode transitions, microwave DBS show what may be the dynamic interaction between geodesic acoustic modes (GAMs) and low-frequency zonal flows (ZF) preceding the L-to-H transition as the turbulence and flows alternately grow and damp in a predator-prey-like interaction [36,37], eventually locking in at the final L-H transition. DIII-D H-mode transition data have also been incorporated into an updated multi-machine database [38].
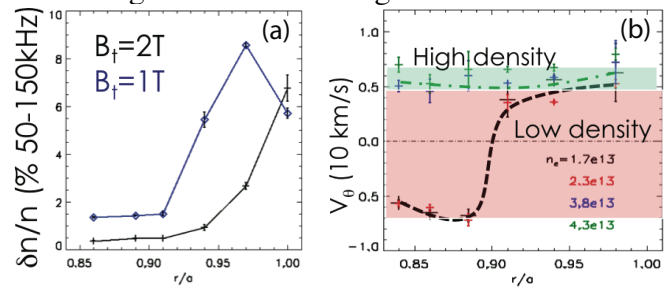

Fig. 13. BES data. (a) higher B_{tor} reduces GAM turbulence. (b) Higher low frequency flow velocity shear at low density prior to H-mode.

The ability to vary the fast-ion pressure profile and the fraction of trapped/passing ions using OANBI, coupled with a comprehensive diagnostic set, provides an excellent set of tools for exploring fast-ion physics. Using off-axis injection to vary the fast ion pressure gradient ($\nabla\beta_f$) near q_{min}, where reversed-shear Alfvén Eigenmodes (RSAEs) are unstable shows stabilization of RSAEs as the OANBI reduces $\nabla\beta_f$, as expected [39,40]. In related studies, we find that resistive wall mode (RWM) stability is improved by off-axis NBI [41]. Finally, in another important test of fast-ion physics, the fast-ion losses produced by the DIII-D ITER TBM mockup coil were measured using an infrared camera, and the data compared with predictions from four different orbit-following simulation codes for cases with a wide variety of EP sources (co-counter and on-off axis NBI). Results show that vacuum field calculations are sufficient to calculate the EP losses and that plasma response does not play a role in prompt loss of these fast ions [42].

6. Research on the Path to Fusion Energy

Significant off-axis current drive capability has been added to DIII-D in order to evaluate advanced configurations having broad current and pressure profiles capable of high β_N fully noninductive steady-state tokamak operation [43]. Theory and experiment indicate that broad current profiles peaked off-axis are beneficial for steady state- high performance solutions. This line of research supports both the ITER steady-state mission and future tokamak development.

Successful modification of a DIII-D neutral beam line provides up to 5 MW of adjustable off-axis co-current NBI (OANBI) out of 20 MW total NBI power [44]. The injection radius is adjustable during a single experimental day over the range $0 \le \rho \le 0.5$ for full-size plasmas ($a \sim 0.62$ m). Initial operation verified neutral beam performance with modified grid structures and collimating apertures, and showed that the deposition profile matched design values [45], as shown in Fig 14.

Fig. 14. Off-axis NBI on DIII-D. Left-hand pictures showing Doppler-shifted H_α emission into D_2 gas. Righthand figure shows current drive from beams at the two tilt angles.

Comprehensive measurements show that off-axis neutral beam current drive and fast ion transport agree with numerical simulation [46]. The neutral beam current drive is very sensitive to toroidal field direction, which significantly changes the ratio of trapped to
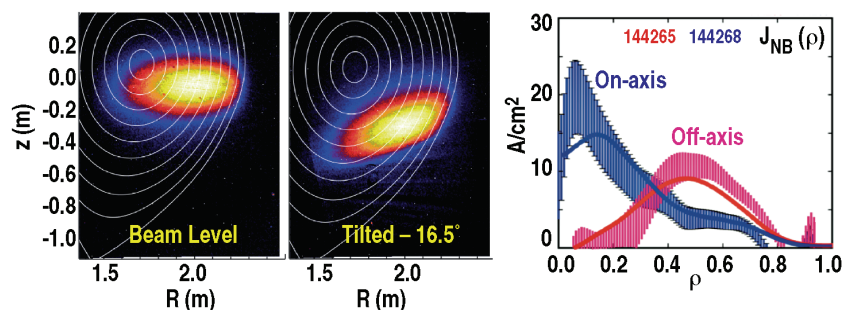
passing particles; "reversed" B_T (I_p and B_T in the same direction) provides 45% more current drive and peaks the current further off axis. Figure 14 shows the NBI current drive inferred from off-axis as compared on-axis current drive using MSE-constrained equilibrium reconstruction; there is good agreement in shape and magnitude with NUBEAM simulation. More extensive studies show no degradation in current drive due to microinstabilities as β increases [46].

The off-axis current drive capabilities enable sustained access to a new range of profiles with sustained minimum safety factors $q_{min}>2$, for durations greater than 2 s [47]. These discharges have broader current profiles (lower l_i) and broader pressure profiles [$P(0)/\langle P\rangle \gtrsim 3$] and significantly higher ideal stability limits than previously obtainable under stationary conditions. These discharges at $B_{tor}=1.8$ T and $\beta_N\sim3$ (Fig. 15) remained well below the calculated beta limit

Fig. 15. Stationary high β_N, high q_{min} discharges maintained with off-axis NBI and ECCD.

($\beta_N>4$). Because $q_{min}>2$, there are no deleterious 2/1 and 3/2 tearing modes, although higher order modes do appear, often as q passes through a rational value. If these modes persist, they can lead to a small decrease in confinement (~15 %). These discharges using off-axis injection are not limited by stability, but rather by available heating power and a somewhat reduced confinement. Because we are interested in fully noninductive discharges in our steady-state research, we do not use counter NBI, limiting the input power to ~15 MW. In addition, although H_{98y2} is still $\gtrsim1$, this value is typically ~20% lower than comparable discharges with on-axis injection and lower q_{min}; an observed increase in Alfvén mode activity might be a contributing factor.

Relaxing q_{min} to 1.5 leads to steady-state discharges with improved confinement at $\beta_N=3.5$ that are close to meeting the requirements for steady-state $Q=5$ operation in ITER and for FNSF-AT ($Q\sim4$) [48]. These discharges have high non-inductive current fractions, $f_{NI}\sim0.7$, and are maintained free of low-order tearing modes by OANBI and ECCD for two current profile relaxation times ($2\tau_R=3$ s), limited by available beam energy (power and pulse length), as shown in Fig. 16. The ECCD (3.2 MW) was applied steadily at $\rho\sim0.4$ and dynamic error field

Fig. 16. Steady-state discharges with off-axis NBI (red) compared to previous results with on-axis NBI only (black).

correction was also used. The safety factor (q_{min} and ρ_{qmin}) and pressure profiles generally agree with FASTRANS simulations [46] that incorporate TGLF transport simulations and realistic heating and current drive inputs. Modest differences are observed between simulation and experiment in $T_e(0)$ (20% higher than measured) and mid-radius T_i profile (steeper computed ∇T_i across $\rho\sim0.2$–0.3).

Further studies using neon injection have explored integrated plasma-based divertor solutions combining enhanced edge and divertor radiation. Initial experiments using neon injection in the divertor of high beta ($\beta_N=3$) $q_{min}=1.5$ Advanced Tokamak discharges doubled the radiative loss from the edge and divertor without degrading confinement ($H_{89p}=2.4$), reducing peak divertor heat flux by ~40%. Future experiments will utilize divertor pumping to control the neon content.

Future steady state fusion devices will place higher demands on plasma facing components, and new integrated core-edge-divertor solutions will be needed. Very promising results were obtained using the snowflake (SF) divertor configuration to significantly reduce inter-ELM peak heat flux (Fig. 17) as compared to a standard single-null divertor. Using only the external poloidal field coils, the SF divertor configuration [49] enables a much larger SOL volume near the x-point, larger divertor contact area (3–4x), and longer parallel connection length than a standard divertor. Preliminary detachment experiments show a similar threshold density as in the conventional divertor, though the radiative volume appears larger (Fig. 17). Early analysis of a limited number of SF discharges indicates that the energy loss per ELM may be reduced [50].
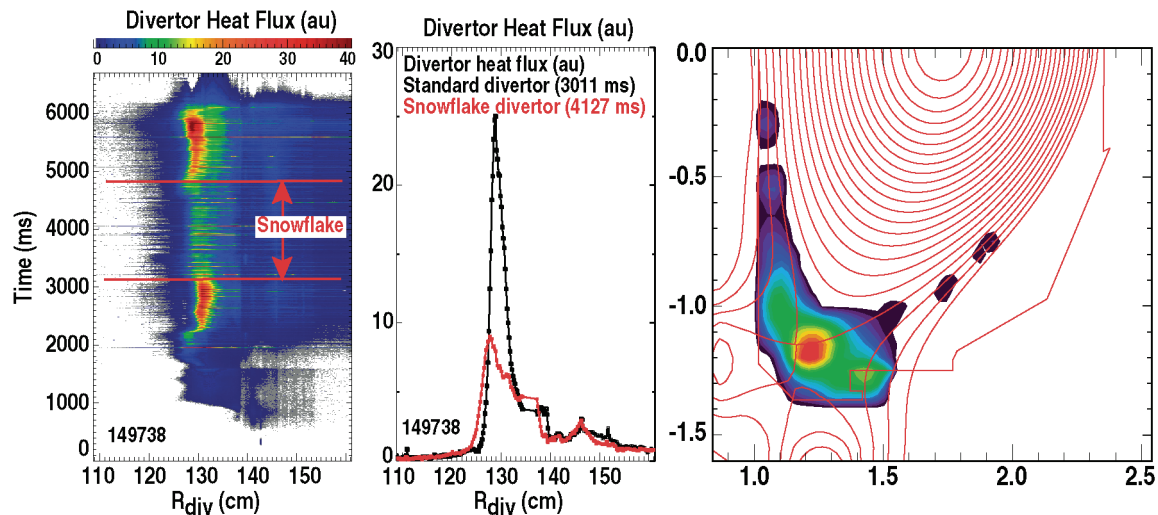

Fig. 17. The snowflake divertor configuration produces a large reduction in peak heat flux with the snowflake configuration. (a) divertor heat flux as function of time; (b) heat flux profiles for standard and snowflake configuration; (c) inversion of bolometer data showing radiative loss during partial detachment following D_2 injection.

A second set of divertor shape experiments varied both the poloidal connection length and the major radius of the outer strike point to test the effect of using the magnetic configuration to change the SOL parallel heat flux while operating in H-mode at fixed density and heating power. Partial detachment using D_2 injection required higher density with increasing R_{div}, contrary to expectations based solely on changing $q_{\parallel}$. The physics behind these variations is being explored with UEDGE [51] and SOLPS modeling [52].

Understanding the magnitude of the divertor challenge is a necessary component in the development of suitable plasma-based solutions. Joint experiments between DIII-D, C-Mod, and NSTX have produced a coordinated multi-machine database relating measured divertor heat flux profiles to H-mode edge pedestal parameters over a wide range of conditions [53]. Scaling analysis shows the peak divertor heat flux scaling as $P_{\mathrm{SOL}}^{1.2} B_{\mathrm{tor}}^{-0.3} B_{\mathrm{pol}}^{-1}$ where P is the SOL power and B_{pol} is the midplane poloidal field at the separatrix. These data were recently combined with data from JET and ASDEX [54] to form a more comprehensive database that confirms this trend, suggesting a much higher parallel SOL heat flux than previously expected in ITER. However, comparison with expected edge-pedestal stability limits suggests simple extrapolation is overly pessimistic [53].

The all-carbon plasma facing components in DIII-D make it possible to measure the gross and net surface erosion rates of tungsten in the divertor under realistic conditions using the DiMES divertor material exposure system. By exposing well-characterized tungsten samples in DIII-D ELMing H-mode plasmas and measuring the change in areal surface density of tungsten, it was possible to determine both the total sputtering and net erosion from the sample, as well as the amount of tungsten redeposited nearby. The data shows that the bulk of

the sputtered tungsten was promptly deposited, in agreement with DIVIMP simulation [55] and consistent with expected lifetime in ITER.

7. Summary and Future Plans

In this paper we have described recent DIII-D research in a number of areas pertinent to successfully completing design, construction, and operation of ITER, and which support the development of steady-state tokamak reactors.

Simulated Q=10 ITER discharges with low applied torque show that achieving required performance is possible while using active feedback ECCD for tearing mode control. Advances in pellet pacing and RMP physics move these ELM control techniques closer to ITER design requirements while strengthening the physics basis for their application; high confinement ELM-free QH-mode can now be obtained over a wide range of applied NBI co- and counter-I_P torque using external n=3 coils. Disruption mitigation experiments point to the possibility of benign runaway electron dissipation with massive gas injection even when well below the Rosenbluth limit.

DIII-D experiments continue to advance the scientific basis to fully exploit ITER by increasing predictive capability for further optimization. Many aspects of the EPED model describing the H-mode pedestal have been confirmed and are now informing ELM control experiments. Deployment of a comprehensive set of fast-ion diagnostics, along with OANBI and new 2D fluctuation measurements, has enabled comprehensive tests of simulation codes that will be used to interpret fast-ion stability and transport in ITER.

Off-axis neutral beam injection is providing new capability for advancing research aimed toward steady-state high-beta Advanced Tokamak operation needed for fusion energy development. Such operating modes are envisioned for ITER and could form the basis of a future Fusion Nuclear Science Facility (FNSF-AT) [48]. Off-axis neutral beam injection has enabled operation with q_{min}>2 to avoid the most unstable tearing modes, measurably broadened the current profile, and sustained high β discharges for more than twice the current relaxation time. In parallel, DIII-D is exploring innovative divertor solutions to address the challenge of steady-state power and particle control.

Future plans seek increased EC power for heating and current drive to improve access to regimes with dominant electron heating, and to improve capability for developing steady-state operating regimes for long-pulse superconducting tokamaks and burning plasma experiments. Commissioning of a 7th long-pulse gyrotron is now under way, with proposed installation of two additional gyrotrons by 2014 to provide increased ECCD power. Other upgrade plans call for additional 3D coil sets and related power supplies in following years. Ongoing modification of existing neutral beam lines to allow longer pulse lengths will continue in the near term. In the future, we plan to tilt a second beam line and increase the operating voltage of the off-axis beams to increase capability for Advanced Tokamak research.

References

[1]   CAMPBELL, D.C. , https://burningplasma.org/ref/ITPACC_campbell_dec11.pdf
[2]   EVANS, T.E., et al., Phys. Rev Lett. **92** (2004) 235003
[3]   EVANS, T.E., et al., this conference, ITR/P1-25
[4]   BAYLOR, L.R., et al., this conference, EX/6-2
[5]   BURRELL, K.H., et al., Phys. Plasmas **8** (2001) 2153
[6]   WADE, M.R., et al., this conference, EX/3-1
[7]   SUTTROP, W., et al., Phys. Rev. Lett. **106** (2011) 225004
[8]   FUTATANI, S., et al., this conference, ITR/P1-22
[9]   SNYDER, P.B., et al., Phys. Plasmas **19** (2012) 056115

[10] SNYDER, P.B., et al., this conference, TH/P3-17
[11] YAN, Z., et al., Phys. Rev. Lett. **107** (2011) 214301
[12] FERRARO, N.M., et al., this conference, TH/P4-21
[13] McKEE, G.R., et al., this conference, EX/P7-06
[14] ROSENBLUTH, M.N. and PUTVINSKI, S.V., Nucl. Fusion **37** (1997) 1355
[15] HOLLMANN, E.M., et al., Nucl. Fusion 51, 103026 (2011)
[16] HOLLMANN, E.M., et al., this conference, EX/9-2
[17] EIDIETIS, N.W, Phys. Plasmas **19** (2012) 056109
[18] JACKSON, G.L., et al., this conference, EX/P2-08
[19] SOLOMON, W.M., et al., this conference, EX/P2-01
[20] BURRELL, K.H., et al., this conference, EX/P4-08
[21] GAROFALO, A.M., et al., 39th EPS Conf Cont Fusion, Stockholm, SE, 2012
[22] KOLEMEN, E., et al., this conference, "State-of-the-Art Neoclassical Tearing Mode Control in DIII-D Using Real-time Steerable Electron Cyclotron Current Drive Launchers," post-deadline submission
[23] NAGASAKI, K., et al., Nucl. Fusion **43** (2003) L7
[24] CHAPMAN, I.T., et al., this conference, ITR/P1-31
[25] SHAFFER, M.J., et al., Nucl. Fusion **51** (2011) 103028
[26] BUTTERY, R.J., et al., this conference, EX/P4-31
[27] REIMERDES, H., et al., this conference, EX/P4-09
[28] GROEBNER, R.J., et al., this conference, EX/11-4
[29] LUCE, T.C., et al., this conference, EX/P3-18
[30] HILLESHEIM, J.C., et al., Proc. 39th EPS Conf. on Cont Fusion, Stockholm, SE, 2012
[31] HOLLAND, C., et al., this conference, EX/P7-09
[32] RHODES, T.L., personal communication, September 2012
[33] SOLOMON, W.M., et al., Nucl. Fusion **51** (2011) 073010
[34] GRIERSON, B.A., et al., this conference, EX/P3-9
[35] YAN, Z., et al., this conference, EX/P7-05
[36] SCHMITZ, L., et al., this conference, EX/P7-17
[37] TYNAN, G., et al., this conference, EX/10-3
[38] GOHIL, P., et al., this conference, ITR/P1-36
[39] TOBIAS, B.J., et al., Phys. Rev Lett. **106** (2011) 075003
[40] HEIDBRINK, W.W., et al., this conference, EX/P6-22
[41] HANSON, J.M., et al., this conference, EX/P4-27
[42] KRAMER, G.J., et al., this conference, ITR/P1-32
[43] LUCE, T.C., Phys. Plasmas **18** (2011) 030501
[44] Murphy, C.J., et al., Proc. of 24th IEEE/NPSS Symp. on Fusion Engineering, Chicago, IL (2011)
[45] VAN ZEELAND, M.A., et al., Proc. 39th EPS Conf. Plasma Physics, Stockholm (2012)
[46] PARK, J.M., et al., this conference, EX/P2-13
[47] HOLCOMB, C.T., et al., this conference, EX/1-5
[48] GAROFALO, A.M., et al., this conference, FTP/P7-35
[49] RYUTOV, D., Phys. Plasmas **14** (2007) 064502
[50] ALLEN, S.L., et al., this conference, "Initial Snowflake Divertor Physics Studies on DIII-D," post-deadline submission
[51] HILL, D.N., et al., J. Nucl. Mater. **415** (2011) S570
[52] PETRIE, T.W., et al., this conference, EX/P5-12
[53] MAKOWSKI, M.A., et al., this conference, EX/P5-16
[54] EICH, T., et al, et al., this conference, ITR/1-1
[56] RUDAKOV, D.L., et al., this conference, EX/P5-11

APPENDIX: THE DIII–D TEAM

G.Abla,[1] S.Aekaeslompolo,[2] R.Akers,[3] S.L.Allen,[4] V.Amoskov,[5] P.M.Anderson,[1] C.Angioni,[6] M.E.Austin,[7] C.Bae,[8] J.P.Bakalarski,[1] C.P.Ballance,[9] J.E.Barton,[10] E.M.Bass,[11] D.Battaglia,[12] C.B.Baxi,[1] L.R.Baylor,[13] M.Becoulet,[14] E.A.Belli,[1] H.Berk,[7] J.W.Berkery,[15] M.N.A.Beurskens,[3] J.M.Bialek,[15] N.Bisai,[16] J.A.Boedo,[11] I.N.Bogatu,[17] R.L.Boivin,[1] P.Bonoli,[18] J.E.Boom,[19] A.H.Boozer,[15] A.Bortolon,[20] M.D.Boyer,[10] B.D.Bray,[1] D.P.Brennan,[21] S.Brezinsek,[22] N.H.Brooks,[1] J.N.Brooks,[23] C.Brunkhorst,[12] D.Buchenauer,[24] R.V.Budny,[12] R.Bulmer,[4] K.H.Burrell,[1] R.J.Buttery,[1] P.Cahyna,[25] J.D.Callen,[26] R.W.Callis,[1] G.L.Campbell,[1] J.M.Candy,[1] J.M.Canik,[13] T.N.Carlstrom,[1] T.A.Carter,[27] W.P.Cary,[1] T.A.Casper,[28] M.Cengher,[1] C.D.Challis,[3] F.R.Chamberlain,[1] V.S.Chan,[1] C.S.Chang,[12] C.S.Chang,[29] I.T.Chapman,[3] A.Chattopadhyay,[16] J.A.Chavez,[1] L.Chen,[20] Y.Chen,[30] H.K.Chiu,[1] M.Choi,[1] M.Chowduri,[16] C.Chrobak,[1] C.Chrystal,[11] M.S.Chu,[1] V.Chuyanov,[28] I.G.J.Classen,[31] R.H.Coen,[4] B.Cohen,[4] A.J.Cole,[15] S.K.Combs,[13] N.Commaux,[13] W.A.Cooper,[32] N.A.Crocker,[27] G.Cunningham,[3] S.daGraca,[33] R.Daniel,[16] J.W.Davis,[34] E.delaLuna,[35] J.C.DeBoo,[1] J.S.deGrassie,[1] S.J.DePasquale,[12] T.M.Deterly,[1] A.Diallo,[12] P.H.Diamond,[11] S.Diem,[13] J.L.Doane,[1] C.W.Domier,[36] A.J.H.Donne,[19] D.Donovan,[24] M.A.Dorf,[4] M.R.Dorr,[4] E.J.Doyle,[27] N.W.Eidietis,[1] J.D.Elder,[34] R.Ellis,[4] R.A.Ellis,[12] R.F.Ellis,[37] T.E.Evans,[1] Y.Feng,[38] M.E.Fenstermacher,[4] N.M.Ferraro,[1] J.R.Ferron,[1] D.K.Finkenthal,[39] R.K.Fisher,[1] S.M.Flanagan,[1] J-P.FloydII,[8] R.J.Fonck,[26] E.Fredd,[12] H.G.Frerichs,[22] A.Fukuyama,[40] S.Futatani,[28] J.Garcia,[14] M.García-Muñoz,[6] A.M.Garofalo,[1] R.Geer,[4] K.W.Gentle,[7] S.Gerhardt,[12] G.Giruzzi,[14] P.Gohil,[1] N.N.Gorelenkov,[12] M.Gorelenkova,[12] Y.A.Gorelov,[1] R.H.Goulding,[13] D.L.Green,[13] K.L.Greene,[1] C.M.Greenfield,[1] N.L.Greenough,[12] Y.Gribov,[28] B.A.Grierson,[12] R.J.Groebner,[1] W.H.Grosnickle,[1] H.J.Grunloh,[1] W.Guo,[41] T.J.Guzman,[1] A.A.Haasz,[34] T.S.Hahm,[12] S.H.Hahn,[42] M.J.Hansink,[1] G.R.Hanson,[13] J.M.Hanson,[15] J.H.Harris,[13] R.W.Harvey,[43] A.Hassanein,[23] N.Hayashi,[44] C.C.Hegna,[26] W.W.Heidbrink,[20] D.N.Hill,[4] J.C.Hillesheim,[27] D.L.Hillis,[13] J.A.Hittinger,[4] G.T.Hoang,[14] C.T.Holcomb,[4] C.Holland,[11] E.M.Hollmann,[11] K.L.Holtrop,[1] M.Honda,[44] R.M.Hong,[1] A.Horton,[13] J.C.Hosea,[12] N.T.Howard,[18] J.Howard,[45] D.M.Hoyt,[1] A.Hubbard,[18] A.Huber,[22] J.W.Hughes,[18] D.A.Humphreys,[1] P.Huynh,[1] G.T.A.Huysmans,[28] A.W.Hyatt,[1] K.Ida,[46] S.Ide,[44] F.Imbeaux,[14] Y.In,[17] R.C.Isler,[13] V.A.Izzo,[11] G.L.Jackson,[1] E.F.Jaeger,[13] Y.M.Jeon,[42] T.C.Jernigan,[13] E.H.Joffrin,[14] R.D.Johnson,[1] S.Joisa,[16] I.Joseph,[4] D.H.Kaplan,[1] K.M.Keith,[1] A.G.Kellman,[1] D.H.Kellman,[1] C.E.Kessel,[12] E.N.Kim,[1] J.S.Kim,[17] J.E.Kinsey,[1] A.Kirk,[3] A.Kirschner,[22] E.Kolemen,[12] M.Kornbluth,[47] T.Koskela,[48] G.J.Kramer,[12] S.I.Krasheninnikov,[11] L.P.Ku,[12] J.A.Kulchar,[1] T.Kurki-Suonio,[48] R.J.LaHaye,[1] B.LaBombard,[18] E.Lamzin,[5] M.J.Lanctot,[4] L.L.Lao,[1] C.J.Lasnier,[4] E.A.Lazarus,[13] E.Le,[7] R.L.Lee,[1] X.Lee,[1] M.Lennholm,[35] A.W.Leonard,[1] J.A.Leuer,[1] G.Q.Li,[41] Z.Lin,[20] A.Litnovsky,[22] C.Liu,[1] Y.Q.Liu,[3] D.Liu,[26] A.Loarte,[28] S.D.Loch,[9] L.L.Lodestro,[4] N.Logan,[12] J.Lohr,[1] J.D.Lore,[13] T.C.Luce,[1] N.C.LuhmannJr.,[36] Y.Ma,[18] M.A.Mahdavi,[49] R.Maingi,[13] M.A.Makowski,[4] R.Manchanda,[16] M.Maraschek,[6] A.Marinoni,[18] L.Marrelli,[50] P.Martin,[50] Y.Martin,[32] G.Matsunaga,[44] P.S.Mauzey,[1] D.C.McCune,[12] W.L.McDaniel,[1] D.C.McDonald,[3] B.B.McHarg,[1] G.R.McKee,[26] A.G.McLean,[4] J.E.Menard,[12] H.Meyer,[3] W.H.Meyer,[4] D.Mikkelsen,[12] D.C.Miller,[1] D.Miller,[12] C.P.Moeller,[1] S.Mordijck,[51] D.Moreau,[14] K.Morris,[4] E.C.Morse,[52] R.A.Moyer,[11] S.H.Müller,[11] J.M.MuñozBurgos,[53] T.Munsat,[30] M.Murakami,[13] C.J.Murphy,[1] C.M.Muscatello,[20] Y-S.Na,[54] A.Nagy,[12] E.Nardon,[14] M.F.F.Nave,[55] G.A.Navratil,[15] R.Nazikian,[12] S.Noraky,[1] R.E.Nygren,[24] R.C.O'Neill,[1] Y.K.Oh,[42] S.Ohdachi,[46] T.Oikawa,[28] M.Okabayashi,[12] A.Okamoto,[56] R.A.Olstad,[1] D.M.Orlov,[11] T.H.Osborne,[1] Y.Ou,[10] L.W.Owen,[13] N.Oyama,[44] N.A.Pablant,[12] D.C.Pace,[1] C.Pan,[41] H.Pandya,[16] A.Y.Pankin,[10] G.Park,[42] H.K.Park,[57] J.K.Park,[12] J.M.Park,[13] C.T.Parker,[1] S.Parker,[30] P.B.Parks,[1] C.J.Pawley,[1] W.A.Peebles,[27] B.Pegourie,[14] B.G.Penaflor,[1] P.I.Petersen,[1] T.W.Petrie,[1] C.C.Petty,[1] N.Q.Pham,[1] V.Philipps,[22] A.Y.Pigarov,[11] D.A.Piglowski,[1] R.I.Pinsker,[1] P.Piovesan,[50] L.Piron,[50] R.A.Pitts,[28] A.Polevoi,[28] P.A.Politzer,[1] D.M.Ponce,[1] M.Porkolab,[18] G.D.Porter,[4] R.Prater,[1] J.P.Qian,[41] R.Rajpal,[16] N.Ramasubramanian,[16] D.A.Rasmussen,[13] H.Reimerdes,[32] D.Reiter,[22] Q.L.Ren,[41] T.L.Rhodes,[27] T.D.Rognlien,[4] J.C.Rost,[18] D.L.Rudakov,[11] P.M.Ryan,[13] D.Ryutov,[4] S.Saarelma,[3] S.A.Sabbagh,[15] G.Saibene,[58] A.Salmi,[48] U.Samm,[22] B.S.Sammuli,[1] M.E.Sawan,[26] M.J.Schaffer,[1] D.P.Schissel,[1] D.J.Schlossberg,[26] O.Schmitz,[22] L.Schmitz,[27] P.Schneider,[6] E.Schuster,[10] E.Scime,[59] J.T.Scoville,[1] M.Shapiro,[18] S.Sharapov,[3] W.Shi,[10] K.Shinohara,[44] K.C.Shoolbred,[1] P.E.Sieck,[1] A.C.C.Sips,[6] R.D.Smirnov,[11] J.P.Smith,[1] S.P.Smith,[1] D.R.Smith,[26] J.A.Snipes,[28] P.B.Snyder,[1] E.R.Solano,[60] W.M.Solomon,[12] A.C.Sontag,[13] A.Soppelsa,[50] K.H.Spatschek,[61] D.A.Spong,[13] R.Srinivasan,[16] H.E.St.John,[1] W.M.Stacey,[8] G.M.Staebler,[1] R.D.Stambaugh,[1] P.C.Stangeby,[34] R.Stemprok,[1] T.Stevenson,[12] H.Stoschus,[53] E.J.Strait,[1] L.Sugiyama,[18] W.Suttrop,[6] Y.Suzuki,[46] V.Svidzinski,[17] T.Tala,[2] P.Tamain,[14] K.Tanaka,[46] R.Tanna,[16] D.A.Taussig,[1] P.L.Taylor,[1] T.S.Taylor,[1] G.Taylor,[12] D.Temple,[3] J.L.Terry,[18] D.M.Thomas,[1] B.J.Tobias,[12] J.F.Tooker,[1] D.Truong,[26] C.K.Tsui,[34] F.Turco,[15] A.D.Turnbull,[1] G.R.Tynan,[11] E.A.Unterberg,[13] I.U.Uzun-Kaymak,[26] M.A.VanZeeland,[1] S.Visser,[1] I.Voitsekhovitch,[3] F.A.Volpe,[15] A.vonHalle,[12] M.R.Wade,[1] M.L.Walker,[1] R.E.Waltz,[1] W.R.Wampler,[24] G.Wang,[27] J.G.Watkins,[24] W.P.Wehner,[10] A.S.Welander,[1] J.C.Wesley,[1] R.B.White,[12] A.E.White,[18] D.G.Whyte,[18] S.Wiesen,[22] TWilks,[8] J.R.Wilson,[12] H.R.Wilson,[62] A.Wingen,[13] E.Wolfrum,[6] C.P.C.Wong,[1] W.Wu,[1] S.J.Wukitch,[18] B.J.Xiao,[41] X.Xu,[4] Z.Yan,[26] H.H.Yip,[1] S-W.Yoon,[42] J.H.Yu,[11] Q.P.Yuan,[41] G.S.Yun,[57] L.Zabeo,[28] L.Zeng,[27] W.Zhang,[27] Y.B.Zhu,[20]

AFFILIATIONS

[1]General Atomics
[2]Association EURATOM-Tekes,Aalto University, Finland
[3]EURATOM/CCFE Fusion Association, Culham Science Centre
[4]Lawrence Livermore National Laboratory
[5]D.V. Efremove Institute, St. Petersburg, Russia
[6]Max Plank Institut für Plasmaphysik, Garching
[7]University of Texas at Austin
[8]Georgia Institute of Technology
[9]Auburn University
[10]LeHigh University
[11]University of California San Diego
[12]Princeton Plasma Physics Laboratory
[13]Oak Ridge National Laboratory
[14]Associatione Euratom CEA, CEA/DSM/IRFM, Cadarache
[15]Columbia University
[16]Institute for Plasma Research, India
[17]FAR-TECH, Inc.
[18]Massachusetts Institute of Technology
[19]Association EURATOM-FOM Rijnhuizen, The Netherlands
[20]University of California Irvine
[21]University of Tulsa
[22]EURATOM-FZ Jülich
[23]Purdue University
[24]Sandia National Laboratories
[25]IPP, AS CR, EURATOM/IPP.CR, Prague
[26]University of Wisconsin-Madison
[27]University of California Los Angeles
[28]ITER Organization, Cadarache
[29]Courant Institute, New York University

[30]CIPS, University of Colorado, Boulder
[31]Dutch Institute for Fundamental Energy Research
[32]CRPP-EPFL-Lausanne
[33]Association EURATOM-IST, Lisbon
[34]University of Toronto
[35]JET-EFDA-CSU, Abingdon, UK
[36]University of California, Davis
[37]University of Maryland
[38]Max Plank Institut für Plasmaphysik, Greifswald
[39]Palomar College
[40]Kyoto University, Japan
[41]ASIPP-Hefei
[42]National Fusion Research Institute, Korea
[43]CompX
[44]Japan Atomic Energy Agency (JAEA)
[45]Australian National University
[46]National Institute for Fusion Studies
[47]Yeshiva University, New York, NY
[48]Helsinki University of Technology
[49]ALITRON
[50]Consorzio RFX
[51]College of William and Mary, Williamsburg
[52]University of California Berkeley
[53]Oak Ridge Institute of Science Education
[54]Seoul National University, Korea
[55]EURATOM Lisbon
[56]Tohoku University, Sendai, Japan
[57]Pohang University of Science & Technology, Korea
[58]Fusion for Energy Joint Undertaking, Barcelona
[59]West Virginia University
[60]Association EURATOM-CIEMAT, Madrid
[61]Heinrich-Heine University, Düsseldorf
[62]University of York